Selective Activation of TASK-3-containing K^+ Channels Reveals Their Therapeutic Potentials in Analgesia

Ping Liao[1*], Yunguang Qiu[3,8*], Yiqing Mo[2*], Jie Fu[2*], Zhenpeng Song[1*], Lu Huang[1*], Suwen Bai[4], Yang Wang[4], Jia-Jie Zhu[5], Fuyun Tian[3], Zhuo Chen[1], Nanfang Pan[1], Er-Yi Sun[1], Linghui Yang[1], Xi Lan[3], Yinbin Chen[2], Dongping Huang[2], Peihua Sun[6], Lifen Zhao[3], Dehua Yang[3], Weiqiang Lu[2], Tingting Yang[7], Junjie Xiao[7], Wei-Guang Li[5], Zhaobing Gao[3], Bing Shen[4], Qiansen Zhang[2], Jin Liu[1], Hualiang Jiang[3,8], Ruotian Jiang[1†], Huaiyu Yang[2†]

[1]Laboratory of Anesthesia and Critical Care Medicine, Department of Anesthesiology, Translational Neuroscience Center, West China Hospital of Sichuan University, Chengdu 610000, Sichuan, China.

[2]Shanghai Key Laboratory of Regulatory Biology, Institute of Biomedical Sciences, School of Life Sciences, East China Normal University, Shanghai 200241, China.

[3]State Key Laboratory of Drug Research and CAS Key Laboratory of Receptor Research, Shanghai Institute of Materia Medica, Chinese Academy of Sciences, Shanghai 201203, China.

[4]Department of Physiology, Anhui Medical University, Hefei 230032, Anhui, China.

[5]Collaborative Innovation Center for Brain Science, Department of Anatomy and Physiology, Shanghai Jiao Tong University School of Medicine, Shanghai 200025, China.

[6]Jiangsu Key Laboratory of Neuropsychiatric Diseases and College of Pharmaceutical Sciences, Soochow University, Suzhou, Jiangsu 215123, China

[7]Cardiac Regeneration and Ageing Lab, School of Life Science, Shanghai University, Shanghai 200444, China.

[8]University of Chinese Academy of Sciences, Beijing 100049, China

[*] These authors contributed equally to this work.

[†]Corresponding authors. hyyang@bio.ecnu.edu.cn for H.Y.; ruotianjiang@scu.edu.cn for R.J..

ABSTRACT

The paucity of selective agonists for TASK-3, a member of two-pore domain K^+ (K2P) channels, has contributed to our limited understanding of its biological functions. By targeting a novel druggable transmembrane cavity using a structure-based drug design approach, we discovered a biguanide compound, CHET3, as a highly selective allosteric activator for TASK-3-containing K2P channels, including TASK-3 homomer and TASK-3/TASK-1 heteromer. CHET3 displayed unexpectedly potent analgesic effects *in vivo* in a variety of acute and chronic pain models in rodents that could be abolished by pharmacology or genetic ablation of TASK-3. We further found that TASK-3-containing channels anatomically define a unique subset population of small-sized, TRPM8, TRPV1 or tyrosine hydroxylase-positive nociceptive sensory neurons and functionally regulate their membrane excitability, supporting CHET3 analgesia in thermal hyperalgesia

and mechanical allodynia under chronic pain. Overall, our proof-of-concept study reveals TASK-3-containing K2P channels as a novel druggable target for treating pain.

One Sentence Summary: Identification of a novel drug target and its new hit compounds for developing new-generation non-opioid analgesics.

INTRODUCTION

Currently available analgesics do not completely treat pain, and some of these analgesics, particularly opioids, provoke social problems (*1*). Thus, discovering new therapeutic targets for developing new-generation analgesics is an urgent need. In particular, targets that treat a variety of pain with similar potency but fewer side effects than μ-opioid receptors are keenly awaited. In this regard, two-pore domain K^+ (K2P) channels hold great promise (*2*) because they produce background leak K^+ currents (*3*) and the activation of which in nociceptors theoretically inhibits pain signaling (*4-6*). The expression of TASK-3 (*Kcnk9*), a K2P channel, has been detected in the peripheral and central nervous system (*7, 8*), including in human dorsal root ganglia (*9*). Recent evidence has suggested that TASK-3 is involved in the perception of cold (*10*), and variations in the *Kcnk9* gene are associated with breast pain in breast cancer patients (*11*). However, its functional and anatomical involvement in chronic pain remains largely

unknown. More importantly, the paucity of selective agonists limits the drug target validation of TASK-3, leaving the notion that selective activation of TASK-3 alleviates pain remains to be tested experimentally. Here, we sought to discover selective activators for TASK-3 and to use the activators as tool compounds to reveal the translational potentials and the underlying mechanisms of TASK-3 in treating pain.

RESULTS

Discovery of the selective activator CHET3 for TASK-3-containing channels

We set out to discover selective activators for TASK-3 via structure-based virtual screening. Since no crystal structure of TASK-3 has yet to be determined, we sought to build a structural model using homology modeling. First, a crystal structure was chosen as the template. To this end, Fpocket 2.0 server (*12*) was applied to detect pockets in the reported crystal structures of K2P channels. In this computation, a druggability score greater than 0.5 (the threshold) means the pocket might be druggable. We found that the cavity under the intracellular side of the filter and the nearby crevice between TM2 and TM4 in four crystal structures (with PDB codes 4RUE, 3UKM, 4XDK and 4XDL) (*13-15*) had druggability scores greater than 0.5 (fig. S1). Thus, this cavity may be a drug binding pocket. Among the four crystal structures, the structure of TREK-2 channel (PDB code 4XDL) is a suitable template for building the structural model of TASK-3 because this structure has good sequence identity (31%) and expectation value (3E-32) in the

sequence alignment generated using the BLAST program (blastp algorithm) and the Clustal Omega server (*16, 17*). Moreover, this TREK-2 structure stood out from the template searching results (with the best QSQE value: 0.66) in the SWISS-MODEL server (*18, 19*). Thus, the structural model of TASK-3 was built based on this crystal structure with Modeller (*20*). Then, based on this model, we performed virtual screening targeting the pocket (Fig. 1, A and B) with SPECS and ChemBridge databases. A few hits were selected for the whole-cell patch-clamp electrophysiological tests in HEK-293T cells overexpressing recombinant human TASK-3, which led to the discovery of a biguanide compound CHET3, a novel TASK-3 activator (half-maximum effective concentration (EC_{50}) 1.4 ± 0.2 μM, Fig. 1, C to F). CHET3 maximally enhanced TASK-3-mediated K^+ currents by ~4-fold, which could be reversed by washout (Fig. 1D) or with pharmacological blockade by PK-THPP (86 ± 3% inhibition at 0.5 μM, n = 6 cells, representative traces shown in Fig. 1E). PK-THPP is a selective inhibitor for TASK-3 against other K2P and other K^+ channels including potassium voltage-gated channel subfamily A member 5 (Kv1.5), human ether-à-go-go–related gene (hERG) and G protein-activated inward rectifier potassium channel 4 (K_{ATP}) (*21*), and we further showed 0.5 μM PK-THPP was insensitive to voltage-gated K^+ channel subfamily B member 1 (Kv2.1) and large conductance Ca^{2+}-activated K^+ channel (BK) channels (fig. S2). In single-channel recordings by inside-out patches, CHET3 enhanced the channel openings mediated by TASK-3 (Fig. 1, G to J), further supporting that CHET3 directly

activated TASK-3. Increases in open probability were observed in both the inward and outward directions in response to 3 μM CHET3 (Fig. 1J).

In addition to forming homomer channels, the TASK-3 subunit can efficiently form heteromer channels with the TASK-1 subunit (*22*). Electrophysiological assays showed that CHET3 could activate TASK-3/TASK-1 (*23*, *24*) with an EC_{50} value of 2.5 ± 0.2 μM with a reduced maximal efficacy of ~2.4-fold (Fig. 1F), and this activation could also be blocked by PK-THPP (90 ± 2% inhibition at 0.5 μM, n = 5 cells, representative traces shown in fig. S3A). However, CHET3 did not activate TASK-1 channels up to 10 μM (Fig. 1F and fig. S3B). Thus, CHET3 is an activator specific for the TASK-3 homomer and TASK-3/TASK-1 heteromer, two TASK-3-containing channels, with high selectivity against the structurally most related K^+ channel TASK-1. In the subsequent sections, we use TASK-3-containing channels to represent TASK-3 homomer and TASK-3/TASK-1 heteromer.

Next, we further examined the selectivity of CHET3. Electrophysiological assays of several other K2P channels, including TREK-1, TREK-2, TRAAK, TRESK and THIK-1, further supported that CHET3 has high subtype selectivity among the K2P family (Fig. 1K and fig. S3B). Furthermore, we found that 10 μM CHET3 has high selectivity against hERG, Kv2.1 and BK channels, which are three K^+ channels sharing similar filter structure and dynamics with K2P (*25*), as well as transient receptor potential cation channel subfamily M member 8 (TRPM8) and transient receptor potential cation channel

subfamily V member 1 (TRPV1) (Fig. 1L, fig. S3, C to G).

We also excluded agonizing and antagonizing functions of CHET3 on pain-related G protein-coupled receptors (GPCRs) by testing the cellular function of μ-opioid receptor (μOR), 5-hydroxytryptamine receptor 1B (5-HT_{1B}R) and cannabinoid receptor type 1 (CB_1R) upon treatment with 10 μM CHET3 (fig. S4). Collectively, these results indicate that CHET3 is a selective activator of TASK-3-containing channels.

Activation mechanism of CHET3

Binding models derived from docking simulation were optimized by molecular dynamics (MD) simulations (fig. S5), which revealed the predominant binding mode of CHET3 within the pocket (Fig. 2, A and B). We next examined the ligand-channel interactions in this binding mode using mutagenesis experiments and RosettaLigand (*26, 27*). Residues T93 and T199 indirectly interacted with CHET3 by water bridges (Fig. 2, A and B). The two residues belong to the filter region, and T93A and T199A mutations led to nonfunctional channels (fig. S6, A and B). F125 may form a π-π interaction with CHET3, and other surrounding residues, including I118, F125, T198, L232, I235, F238 and L239, likely contribute hydrophobic interactions with the ligand. RosettaLigand computations based on this MD mode predicted that the I118A, F125A, L232A, I235A, F238A and L239A mutants decrease CHET3 binding, while the T198A mutant should not (Fig. 2C). Indeed, a saturating concentration of CHET3 (10 μM) showed no activation on F125A, I235A, and F238A mutants and reduced activation on L239A mutant, whereas

CHET3 activated T198A similarly to the wild-type (WT) (Fig. 2D). Mutant L232A is nonfunctional (fig. S6C). Although CHET3 did not show reduced activation on I118A (Fig. 2D), the experimental results are generally consistent with the computational predictions. To gain further insight into the action mechanism of CHET3, MD simulations were carried out on *apo* TASK-3 for comparison with CHET3-bound TASK-3 (Fig. 2, E and F). In two out of three independent simulations for the *apo* system, the channel selectivity filter tended to stay in a nonconductive-like conformational state (Fig. 2, E and F). In contrast, in all three simulations for the CHET3-bound system, the channel filter adopted a conductive-like state (Fig. 2, E and F). Furthermore, our simulations supported the previous report by González *et al.* that the H98 residue plays a role in modulating the extracellular ion pathway in TASK-3 (*28*). In the simulations of the CHET3-bound TASK-3, H98 adopted a conformation opening the extracellular ion pathway (Fig. 2E and fig. S7A). In contrast, in ligand-free mode, H98 has a high probability of adopting a conformation closing this pathway (Fig. 2E and fig. S7B).

CHET3-induced analgesia in rodents

Next, we systematically evaluated CHET3 in analgesia. The anti-nociceptive effect of CHET3 was first assessed by the tail immersion test at 52 ℃. CHET3 displayed dose-dependent analgesia with a fast onset (30 min) after intraperitoneal (i.p.) injection, with a maximal effect at a dose of 10 mg/kg (Fig. 3A). Hereafter, 10 mg/kg i.p. injection was used for most of the following animal studies. Interestingly, CHET3 was only

164 effective in response to a noxious cold stimulus (5 ℃) or a noxious heat stimuli (46 ℃
165 and 52 ℃) but not to physiological stimuli (20 ℃ and 40 ℃) (Fig. 3A). Importantly, the
166 CHET3 analgesia was fully blocked by the co-administration of PK-THPP, and PK-THPP
167 alone also produced a nociceptive effect in the tail immersion test at 46 ℃ (Fig. 3A).
168 Next, both the early and late phases (*29*) of acute inflammatory pain induced by formalin
169 were attenuated by CHET3 (Fig. 3B), suggesting at least a peripheral effect of CHET3.
170 The paw pressure test revealed that CHET3 reduced mechanical pain in mice, and the
171 effect was fully blocked by PK-THPP (Fig. 3C). Next, we evaluated the analgesic effects
172 of CHET3 on chronic pathological pain. In the spared nerve injury (SNI)-induced
173 neuropathic pain mouse model, CHET3 significantly reduced the frequency of hind paw
174 lifting (Fig. 3D), an indicator of spontaneous/ongoing pain behavior in the SNI model
175 (*30*). In the cold plantar test, CHET3 attenuated the cold hyperalgesia in SNI in the
176 development (SNI 7 d) and maintenance (SNI 14 d and 21 d) stages of chronic pain,
177 which could be reversed by PK-THPP. PK-THPP alone, however, had no effect in the
178 cold plantar test in SNI mice (Fig. 3E). CHET3 was more effective in relieving cold
179 hyperalgesia than pregabalin, a first-line agent for the treatment of neuropathic pain (Fig.
180 3F). In SNI mice, CHET3 had little effect on alleviating mechanical allodynia in the von
181 Frey test. However, in SNI rats, 10 mg/kg CHET3 attenuated mechanical allodynia
182 throughout the different stages of chronic pain in the von Frey test, which could be
183 reversed by PK-THPP (Fig. 3G). PK-THPP alone had no effect on pain in the von Frey

test in SNI rats (Fig. 3G). The analgesic effect of CHET3 at a dose of 20 mg/kg exhibited a faster onset (30 min post injection) with similar efficacy to 10 mg/kg CHET3 (fig. S8) in the von Frey test in SNI rats. In chronic inflammatory pain induced by the Complete Freund's Adjuvant (CFA), CHET3 reduced heat hyperalgesia in the Hargreaves test, which was blocked by PK-THPP (Fig. 3H). In addition, PK-THPP injection alone aggravated heat hyperalgesia (Fig. 3H).

Chronic pain may induce anxiety (*31, 32*). Compared with Sham mice, SNI mice spent less time in open arms in the elevated plus maze test and spent less time in the light box in the light/dark box test, suggesting anxiety-like behaviors in the SNI mice. The administration of CHET3 30 min before the test significantly alleviated anxiety-like behaviors in both tests (Fig. 3, I and J). Together, our data suggest that CHET3 potently and efficaciously attenuated acute and chronic pain and pain-associated anxiety in rodents, and the analgesic effects of CHET3 could be pharmacologically blocked by the TASK-3 blocker PK-THPP. Importantly, CHET3 had no effects in grip strength, rotarod and open field tests (fig. S9, A to C), suggesting that CHET3 had no effect on the locomotion activities in mice. Since TASK-3 was found to be expressed in mouse carotid boy type-1 cells (*33*), we also evaluated the possible side effects of CHET3 on cardiovascular function in mice or rats. We monitored blood pressure and heart functions using echocardiography, and we did not observe any significant change in blood pressure (fig. S9, D to F) or heart functions including Ejection Fraction (EF) and Fractional Shortening

(FS) (table S1) in a post-injection time window between 45 min–90 min, during which CHET3-induced analgesia peaked in most cases. We also monitored the change in body temperature following CHET3 systemic administration, and no significant hyperthermia or hypothermia was observed (fig. S9G).

Further on-target validation using chemical and genetic approaches

Was CHET3 truly targeting TASK-3 containing K^+ channels as an analgesic? We next performed additional target validation experiments using chemical and genetic approaches. Medicinal chemistry yielded CHET3-1 and CHET3-2 (Fig. 4A), two derivatives of CHET3. In the CHET3-TASK-3 binding model (Fig. 2, A and B), the dioxane ring may form a π–π interaction with the F125 residue. CHET3-1, in which the dioxane ring is replaced with an aromatic ring, should maintain the π–π interaction. CHET3-2 should lose the π–π interaction since the dioxane ring is replaced by a steric bulk *tert*-butyl group. Binding energy computations based on the binding model suggested that the binding affinity of CHET3-1 to TASK-3 was similar to that of CHET3, while that of CHET3-2 decreased (fig. S10). In accordance, CHET3-1 activated TASK-3 with an EC_{50} value of 0.5 ± 0.1 μM, while CHET3-2 was inactive (Fig. 4B), further supporting the putative binding model. We reasoned that CHET3-1 should be bioactive in analgesia, whereas CHET3-2 should not, if CHET3 truly targets TASK-3-containing channels to act as an analgesic. Indeed, CHET3-1 attenuated cold hyperalgesia in SNI mice (Fig. 4C), mechanical allodynia in SNI rats (Fig. 4D), and heat hyperalgesia in CFA

mice (Fig. 4E), and all of these effects could be reversed by PK-THPP (fig. S11). In contrast, CHET3-2 was completely inactive in all the experiments above (Fig. 4, C to E).

We also generated *Kcnk9* gene knockout (TASK-3 KO) mice (fig. S12). Knocking out *Kcnk9* should abolish the function of TASK-3 homomer and TASK-3/TASK-1 heteromer *in vivo*. In TASK-3 KO mice and WT control mice, we measured the basal sensitivity to nociception, thermal hyperalgesia and mechanical allodynia, and we also evaluated the analgesic effect of CHET3 in these mice. Tail immersion (Fig. 5, A and B), paw pressure tests (Fig. 5C) and von Frey tests in naïve animals (Pre SNI, Fig. 5D) did not reveal any significant difference in baseline nociceptive sensitivity between TASK-3 KO and WT; however, cold plantar (Pre SNI, Fig. 5F) and Hargreaves tests (Pre CFA, Fig. 5G) revealed increased nociceptive cold and heat sensitivity in TASK-3 KO mice. Furthermore, in the chronic pain models, von Frey, cold plantar and Hargreaves tests revealed that TASK-3 KO mice exhibited aggravated mechanical allodynia (Fig 5D), spontaneous neuropathic pain behavior (Fig. 5E), and thermal hyperalgesia (Fig. 5, F and G). As expected, CHET3 was completely inactive in TASK-3 KO mice in all the tests described above (Fig. 5, A to G). Thus, using tool compounds (Fig. 4) and mouse genetics (Fig. 5), we provide strong evidence showing that CHET3 targets TASK-3-containing channels, thus acting as an analgesic, and the loss of TASK-3 contributed to the generation/maintenance of both acute and chronic pain.

Distribution of TASK-3-containing channels in sensory neurons

Our pharmacokinetic profile of CHET3 (tables S2 and S3) showed a negligible brain concentration of CHET3 and a high concentration of CHET3 in the plasma in both the naïve and SNI 7-d mice, suggesting that CHET3 mainly acted peripherally. The peripheral effect of CHET3 is also supported by the fact that CHET3 attenuated the early phase of formalin-induced pain (Fig. 3B). These findings, along with the previous finding that TASK-3 in dorsal root ganglion (DRG) neurons mediates cold perception (*10*), strongly suggest that peripheral TASK-3-containing channels contribute largely, if not entirely, to the analgesic effects of CHET3. Therefore, we evaluated the TASK-3 functions/distributions in the peripheral nervous system, particularly in DRG.

We used fluorescence in situ hybridization (ISH) (RNAscope technique) to map the mRNA expression of TASK-3 in DRG and trigeminal ganglia (TG). The specificity of the fluorescent signals was validated by a positive control probe and a negative control probe (see the Methods). *Kcnk9* was identified in a subset of neurons (~7% of total neurons) in DRG, predominantly in small-sized neurons (diameter $\leq$ 20 μm) (Fig. 6, A and C), indicative of its specific expression in nociceptors. Interestingly, a much higher expression level of *Kcnk9* (~14% of total neurons) was found in TG (Fig. 6, A and B). In DRG, approximately 95% of *Kcnk9*$^+$ neurons express the TASK-1 subunit, suggesting possible formation of the TASK-3/TASK-1 heteromer in DRG, and approximately 50% of *Kcnk9*$^+$ neurons express TRPV1, a well-known noxious heat sensor predominantly expressed in peptidergic nociceptive sensory neurons (*34*). More than 95% of *Kcnk9*$^+$

neurons express TRPM8, and very little *Kcnk9*$^{+}$ neurons express TRPA1, two well-known noxious cold sensors (*34*). Furthermore, approximately 50% of *Kcnk9*$^{+}$ neurons express tyrosine hydroxylase (TH), a marker for c-low threshold mechanoreceptors (c-LTMRs) predominantly found in nonpeptidergic nociceptors (*35*), whereas *Kcnk9* rarely colocalizes with *P2rx3* (P2X3), which labels mainly TH^{-} negative, IB4^{+} nonpeptidergic nociceptors (*36*), nor does *Kcnk9* colocalize with *Ntrk2* (TrkB), a marker for Aδ-LTMRs (*35*). Thus, TASK-3 marks a unique subpopulation of both peptidergic and nonpeptidergic nociceptive sensory neurons enriched in thermal sensors (TRPV1, TRPM8) or mechanoreceptors (TH^{+} c-LTMRs) (Fig. 6, D to F), in line with its functional involvement in thermal and mechanical sensation *in vivo*. In agreement with a previous study (*37*), we found that *Kcnk9* expression was downregulated in SNI mice and CFA mice (fig. S13), further suggesting that the downregulation of TASK-3-containing channels contributes to the generation/maintenance of chronic pain.

Functional roles of TASK-3-containing channels in nociceptive neurons

The functional roles of TASK-3-containing channels were examined by whole-cell patch-clamp recordings in dissociated DRG neurons. Recordings were focused on small DRG neurons (diameter of ~20 μm, cell capacitance of ~30 pF) based on the ISH data. To isolate K^{+} currents, voltage ramps from -120 mV to -30 mV were applied. In total, 89 cells were recorded, and 16 cells responded to CHET3 (20.3 ± 6.3%, 11 mice). In the CHET3-sensitive cells, CHET3 enhanced the whole-cell current density by

284 approximately 18%, which could be further inhibited by PK-THPP by approximately 38%
285 at -30 mV (Fig. 7A). We subtracted the CHET3-sensitive current, and we found this
286 current was strongly outwardly rectifying and was tiny between -120 mV and -60 mV,
287 leaving the reversal potential of the CHET3-sensitive current difficult to resolve (Fig. 7B).
288 We further sought to isolate current carried by TASK-3-containing channels by
289 subtracting PK-THPP-sensitive current. We consistently found a similar profile for
290 PK-THPP-sensitive current (fig. S14A), further suggesting the low basal conductance at
291 hyperpolarized membrane potentials, while strong outwardly rectifying represents an
292 intrinsic property of K^+ currents mediated by TASK-3-containing channels in DRG under
293 our experimental conditions. To increase the drive force of the K^+ currents in the
294 hyperpolarized potentials, we increased the extracellular K^+ concentration to 143 mM.
295 Under this condition, the CHET3-sensitive current was reversed at approximately 6.7 mV,
296 which was close to the theoretical value of 1.5 mV for K^+ conductance (Fig. 7B).
297 The tiny CHET-3- or PK-THPP-mediated currents at approximately -60 mV suggest
298 that the basal activity of TASK-3-containing channels around the resting membrane
299 potential (RMP) range was low and, thus, that CHET3 or PK-THPP is unlikely to be able
300 to regulate the RMP. To systematically evaluate the regulatory role of CHET3 on the
301 excitability of nociceptive neurons, we first applied a cocktail solution containing
302 menthol and capsaicin, two agonists for TRPM8 and TRPV1 (*38*, *39*), respectively, to
303 better identify the nociceptive neurons that likely express TASK-3-containing channels.

Only neurons responding to the cocktail (fig. S14B) were studied in the subsequent experiments. Consistent with the low activity of TASK-3-containing channels at approximately -60 mV, the application of CHET3 or PK-THPP or vehicle (Control) did not hyperpolarize the RMP; rather, they all slightly depolarized the membrane by ~2 mV with no significant difference among the three groups, suggesting that CHET3 or PK-THPP had no specific roles in altering RMP (Fig. 7C). Next, we explored how CHET3 regulates action potentials. In 12 out of 27 neurons, the application of CHET3 markedly increased the rheobase required to elicit the action potentials (APs) by ~70% and decreased the frequency of APs evoked by suprathreshold current injections by ~65% (Fig. 7, D and E). In the other 15 cells, CHET3 had no effect on the rheobase and slightly increased the frequency of APs evoked by suprathreshold current injections by 10% (fig. S14, C and D). In 7 of these 12 CHET3-sensitive cells, we were able to further apply PK-THPP, which reversed the effects of CHET3 (fig. S14, E and F). Furthermore, in another independent set of experiments, we coapplied CHET3 and PK-THPP in naïve cells. In 11 out of 27 cells, the coapplication of CHET3 and PK-THPP markedly decreased the rheobase by ~40% and increased the frequency of APs evoked by suprathreshold current injections by ~50% (Fig. 7, F and G); in the other 16 cells, coapplication of CHET3 and PK-THPP slightly increased the rheobase by ~20% but had no effect on the AP frequency evoked by suprathreshold current injections (fig. S14, G and H). Collectively, our electrophysiological data suggest the functional presence of K^+

currents mediated by TASK-3-containing channels, the enhancement of which reduces the excitability of nociceptive neurons without affecting the RMP.

Finally, Ca^{2+} imaging experiments were performed in acutely dissociated DRG neurons to measure how the activation of TASK-3-containing channels contributes to the thermal sensitivity of DRG neurons. Thermal stimulations elicited Ca^{2+} signals in a portion of small-sized DRG neurons (Fig. 7H, cells with an F_{340}/F_{380} ratio ≥ 0.2 were considered responding cells shown in black, and those with an F_{340}/F_{380} ratio < 0.2 were considered nonresponding cells shown in gray). We confirmed that these Ca^{2+} signals were temperature-dependent and were mediated by TRP channels because the heat-induced responses could be blocked by 5 μM AMG9810 (TRPV1 antagonist) (*40*) (fig. S15, A and B), and the cool-induced responses could be blocked by 10 μM BCTC (TRPM8 antagonist) (*38*) and 20 μM HC030031 (TRPA1 blocker) (*41*) (fig. S15, A and B). Bath application of 10 μM CHET3 significantly and markedly inhibited the Ca^{2+} signals evoked by cool- or heat- stimulation in small-sized DRG neurons (Fig. 7, H and I), suggesting that the activation of TASK-3-containing channels was able to lower the excitability of the nociceptive neurons in response to external thermal stimulations.

DISCUSSION

The current study has three major findings: First, we discovered selective agonists for TASK-3-containing channels by targeting a transmembrane cavity under the

selectivity filter using structure-based approaches. Second, *in vivo* activation of peripheral TASK-3-containing channels displayed potent analgesia, suggesting a TASK-3-based therapeutic strategy for treating chronic inflammatory and neuropathic pain. Third, our anatomical and functional data highlight the roles of peripheral TASK-3-containing channels in controlling the excitability of nociceptive neurons.

Very recently, Schewe *et al.* reported a class of negatively charged activators (NCAs) that could activate K2P channel, hERG channel and BK channel and revealed that the site below the selectivity filter is the binding site of the NCAs (*25*). In the present work, our virtual screening obtained CHET3, a non-charged compound that acts on this site, further supporting the finding that the site below the selectivity filter is a ligand binding site. It is noteworthy that NCAs are nonselective activators for a variety of K^+ channels, while CHET3 is highly selective for TASK-3-containing channels, suggesting the versatility of this binding site. Additionally, NCAs and CHET3 may share some common activation mechanisms on K2P channels, as they both influence the conformation of the selectivity filter. Notably, the activation mechanism we describe in this study does not fully explain the selectivity of CHET3. In particular, TASK-1 and TASK-3 are the closest relatives to each other, and the residues below the selectivity filter as well as H98 are conserved. Further studies to elucidate the differential responses of TASK-1 and TASK-3 to CHET3 may be helpful for understanding the selective modulation principle in K2P.

In most cases, the initial proof-of-concept identification of a protein as a potential

364 target is dependent on genetic methods. However, genetic deletion may induce
365 modifications to other genes. This off-target genetic side effect discredits target validation
366 work. This is particularly the case in the field of pain medicine: genetically mutated mice,
367 e.g., $Na_v1.7$-null mice and humans exhibited remarkable insensitivity to pain, whereas
368 potent selective antagonists have weak analgesic activity (*42*, *43*). Another example
369 related to the K2P field is that migraine-associated TRESK mutations lead to the
370 inhibition of TREK-1 and TREK-2 through frame shift mutation-induced alternative
371 translation initiation (fsATI) to increase sensory neuron excitability and are linked to
372 migraine (*44*). Using chemical probes to validate targets pave another way for later
373 translational research. Regarding in *vivo* applications of chemical probes in target
374 identification and validation, a major issue is whether the observed phenotypes are indeed
375 relevant to the on-target of the probes. In this study, we provide three independent lines of
376 evidence showing that CHET3 targets TASK-3-containing channels to act as an analgesic.
377 First, the TASK-3 inhibitor PK-THPP could block CHET-3-induced analgesia. Second,
378 two structurally similar analogs were discovered and used in the *in vivo* tests. CHET3-1, a
379 TASK-3 activator structurally similar to CHET3, is bioactive in analgesia, and could also
380 be blocked by PK-THPP. CHET3-2, another analog that is highly structurally similar to
381 CHET3, did not activate TASK-3 and was completely ineffective in all the analgesia tests.
382 Finally, CHET3 had no analgesic effect in TASK-3 KO mice in all the tests. Collectively,
383 our data suggest that the on-target activity of CHET3 is linked to the analgesic

384 phenotypes.

385 Although CHET3 has a higher activation efficacy on TASK-3 over TASK-3/TASK-1,
386 we suggest that both TASK-3 homomer and TASK-3/TASK-1 heteromer channels likely
387 contribute to CHET3-induced analgesia for the following reasons: 1) *Kcnk9* is highly
388 colocalized with *Kcnk3* in DRG; 2) TASK-3/TASK-1 heteromer has been found
389 assembled efficiently and functionally in cerebellar granule cells (*45*), motoneurons (*46*)
390 and carotid body glomus cells (*47*).

391 We found that CHET3 decreased the excitability without changing the RMP of
392 nociceptive neurons. The lack of change in RMP could be explained by the fact that
393 CHET3- or PK-THPP-mediated currents are negligible at approximately –60 mV. One
394 may argue that there may be strong depolarizing "off-target" activity of CHET3 through
395 another unknown channel/receptor, thereby masking the hyperpolarizing effect mediated
396 by CHET3 on TASK-3-containing channels. However, if this were the case, one would at
397 least expect PK-THPP to depolarize the RMP since PK-THPP, a molecule that is
398 structurally distinct from CHET3, is unlikely to produce hyperpolarizing "off-target"
399 activity through the same unknown channel/receptor.

400 CHET3 acted mainly on peripheral TASK-3-containing channels. Peripheral targets
401 are much less likely to produce central side effects, including dependence/addiction.
402 Although the utility of CHET3 and its derivatives as preclinical candidate compounds
403 requires further assessment with systematic nonclinical safety tests performed in GLP

(Good Laboratory Practice) in rodents and other animals, it seems that the activation of peripheral TASK-3-containing channels does not produce obvious severe acute side effects on the cardiovascular system, where TASK-3-containing channels are also expressed. Interestingly, we found that TASK-3 was more highly expressed in TG than in DRG. Further studies are needed to evaluate the translational potentials of TASK-3 activation (TASK-3/TASK-1) in TG to treat chronic pain related to trigeminal neuralgia and migraine. Finally, although TASK-3 is expressed in human DRG (*9*) and variation in *KCNK9* is involved in breast pain in breast cancer patients (*11*), direct evidence for the functional involvement of TASK-3 in pain signaling in humans is lacking. Future functional studies on human tissues or studies with genetic screening of TASK-3-related mutations in humans would greatly aid in assessing the translational potential of TASK-3 for treating pain in humans.

MATERIALS AND METHODS

Study design

Structure-based drug design methods were used to perform initial virtual screening, and patch-clamp electrophysiology was mainly used to study the activity/mechanism of candidate compounds on TASK-3-containing channels. The analgesic effects of TASK-3 activators were then studied in acute and chronic pain models in mice and rats. Pharmacokinetic analysis was performed to assess how CHET3 was distributed. KO mice

were used to confirm the on-target activity of CHET3. Finally, *in situ* hybridization with the RNAscope technique was used to map the distribution of TASK-3 in DRG and TG. The functional roles of TASK-3 were assessed by measuring how CHET3 and PK-THPP modulate K^+ currents, action potential firings and sensitivity to thermal stimulation in nociceptive neurons.

Sample size and replicates: For single-cell based experiments, at least 5 cells per condition were tested. For in *vivo* studies in animals, 6-10 animals per condition were used. No power analysis was performed to determine the sample size.

Homology modeling for the TASK-3 structure

A sequence alignment was generated by using the Clustal Omega server (*16*). Notably, the two pore domains and selectivity filter sequence motifs were highly conserved among the K2P channels, which were largely used to guide the alignment. Conserved residues E30 and W78 in TASK-3 helped to locate the position of the non-conserved cap domain.

Virtual screening

Docking was performed by using Schrödinger Glide software (New York, NY, USA). Compounds were screened using the high-throughput virtual screening (HVS) module followed by the standard docking module SP in Glide. The Glide G-score was used to rank the results list. To allow for diversity of molecular structures, binding modes and drug-like properties, twelve hits were selected for the bioassay.

Chemicals

444 PK-THPP was purchased from Axon Medchem. CHET3 purchased from commercial
445 sources was used in the initial electrophysiological screening. Then, CHET3 was
446 synthesized in the lab for the following studies in this paper. The synthesis routes and
447 characterization of CHET3 and its derivatives CHET3-1 and CHET3-2 are outlined in the
448 Supplementary Materials.

449 For electrophysiology, stock solutions of CHET3 and its derivatives (50 mM) were
450 prepared in dimethyl sulfoxide (DMSO) and diluted in the extracellular solution before
451 use.

452 For animal studies, CHET3 and PK-THPP were both dissolved in 10% DMSO, 5%
453 Tween 80 and 85% saline; CHET3-1 was dissolved in 10% DMSO, 5% ethoxylated
454 castor oil, 35% poly (ethylene glycol) and 50% corn oil; and CHET3-2 was dissolved in
455 14% DMSO, 5% Tween 80 and 81% saline. The solvents were used as vehicle controls.

456 **Detailed modeling of the CHET3-TASK-3 binding poses**

457 Initially, the configuration of CHET3 was determined by the Ligprep module in
458 Schrödinger Maestro and Gaussain09 (Gaussian, Inc). Detailed descriptions are displayed
459 in the Supplementary Materials. The configuration of the tautomer with the lowest energy
460 was adopted to generate multiple ring conformations. CHET3 conformations were
461 docked to the TASK-3 channel model by standard Glide as described for the virtual
462 screening. Two binding modes (G-score values at -8.3 and -7.9, separately) were obtained
463 from docking. In the best pose (1st model in fig. S5A), the guanidyl group in CHET3

464 establishes a hydrogen bond with the backbone NH of residue L232 in TM2, while the
465 guanidyl group in the additional mode of binding (2nd model in fig. S5B) faces towards
466 the selectivity filter and interacts with hydroxyl group of T199. To identify the accurate
467 binding mode of CHET3, two docking models were further studied using molecular
468 dynamics (MD) simulations (see below).

469 **MD simulations**

470 The TASK-3 model obtained from homology modeling and two binding models of
471 CHET3-bound TASK-3 were used to build the models of *apo* TASK-3 and
472 CHET3-bound TASK-3, respectively. Models were inserted in a POPC
473 (1-palmitoyl-2-oleoyl-sn-glycero-3-phosphocholine) lipid bilayer to establish the
474 CHET3-bound system and the *apo* system, respectively. MD simulations were carried out
475 by using GROMACS 5.1.4 (*48*) with CHARMM36 parameters (*49*).

476 **Comparison of the binding of CHET3, CHET3-1 and CHET3-2**

477 The RosettaLigand application (*26, 27*) was applied to dock CHET3, CHET3-1 and
478 CHET3-2. The best binding mode obtained from MD simulations was adopted as the
479 initial docking model. For each docking trial, the top 1000 models were sorted by total
480 score, and the binding energy between three compounds and the channel was calculated.
481 Additionally, *in silico* alanine scans were conducted by individually changing the residue
482 to alanine without otherwise changing the conformation of the protein or ligands in
483 Rosetta. To explore the distribution of binding interactions between compounds and

proteins, the average energies of the top 10 models with the lowest binding energies (interface score) were calculated. To compare the binding of CHET3, CHET3-1 and CHET3-2, the top 50 models of each compound with the lowest binding energies were used to calculate the total score and interface score.

Electrophysiology

Electrophysiology tests of hTASK-3, hTASK-1, hTREK-1, mTREK-2, hTRAAK, hTHIK-1, hTRESK, hTASK-3/hTASK-1, hTRPM8 and hTRPV1 were performed with transiently transfected HEK-293T cells. The cDNAs of hTASK-3, hTASK-1, hTHIK-1, hTRESK and hTASK-3/hTASK-1 were subcloned into the pCDNA3 vector (Invitrogen). The cDNAs of hTREK-1, mTREK-2, hTRAAK, hTRPM8 and hTRPV1 were subcloned into the pEGFPN1 expression vector (Invitrogen). For hTASK-3/hTASK-1, concatemer products were designed for the 3' and 5' ends of TASK-3 and TASK-1, ensuring that the stop codon of TASK-3 was removed.

Electrophysiological tests of hERG, Kv2.1 and BK were performed with stable cell lines. The CHO-hERG stable cell line was generated in-house and was based on a standard CHO-K1 cell line. The HEK293-human Kv2.1 stable cell line and the CHO-human BK stable cell line were generated by Ion Channel Explore (Beijing, China).

Whole-cell recordings of ion channels were performed with patch-clamp amplifiers (EPC10, HEKA or Axon 700B, Molecular Devices) at 23-25 ℃. The current signals were filtered at 2 kHz and digitized at 10 kHz. The pipettes for whole-cell recordings were

pulled from borosilicate glass capillaries (World Precision Instruments) and had a resistance of 3-7 MΩ. For recordings of K^+ channels, the standard pipette solution contained (in mM) 140 KCl, 2 $MgCl_2$, 10 EGTA, 1 $CaCl_2$, and 10 HEPES (pH 7.3, adjusted with KOH), and the external solution contained (in mM) 150 NaCl, 5 KCl, 0.5 $CaCl_2$, 1.2 $MgCl_2$, and 10 HEPES (pH 7.3, adjusted with NaOH). For recordings of the TRPV1 and TRPM8 currents, the internal solution contained (in mM) 140 CsCl, 0.1 $CaCl_2$, 1 $MgCl_2$, 10 HEPES, and 5 EGTA (pH 7.2, adjusted with CsOH), and the external solution contained (in mM) 140 NaCl, 5 KCl, 1 $MgCl_2$, 0.5 EGTA, and 10 HEPES (pH 7.4, adjusted with NaOH). For recordings of hERG, the outward current of hERG channels was elicited by a 2.5-second depolarization step to +30 mV from a holding potential of -80 mV, followed by a 4-second repolarization step to -50 mV to measure the tail current. For recordings of Kv2.1, currents were evoked by a 200-millisecond depolarization step to +60 mV from a holding potential of -80 mV. For recordings of BK, currents were evoked by a 1-second depolarization step to +70 mV from a holding potential of -80 mV. For recordings of TRPV1 and TRPM8, currents were recorded using a ramp protocol from -100 mV to +100 mV over a period of 400 milliseconds at a holding potential of 0 mV.

Single-channel current recording was acquired in the excised inside-out configuration of patch clamp using EPC10 (HEKA) at 23-25 °C. The pipettes had resistances of 7-15 MΩ. The standard pipette and bath solutions contained (in mM) 140 KCl, 1 CaCl2, 2 MgCl2, 10 HEPES and 10 EGTA (pH 7.4, adjusted with KOH). At acquisition the single-channel currents were low-pass filtered at 2 kHz and sampled at 10 kHz.

Recordings lasting at least 50 s were put to further analysis to ensure enough events detected. A threshold at half the open channel current amplitude of the major conductance state was set to detect the single channel events. No junction potential correction was done. All the events in the selected section were detected automatically using Clampfit 10 (Molecular Devices, Inc.) followed by manual inspection. The amplitude histograms were fitted with Gaussian distributions with a bin width of 0.1 pA. TASK3 channel activity in an inside-out patch was expressed quantitatively as NP_O (N is the number of channels in the patch, and P_O is the probability of a channel being open). The NP_O was calculated by the relative area under all points amplitude histogram and expressed as follows:

$$NP_O = (A_1 + 2A_2 + 3A_3 + \ldots + nA_n) / (A_0 + A_1 + A_2 + \ldots + A_n),$$

where A_0 is the area under the Gaussian curve of an all points histogram corresponding to the closed state, $A_1 \ldots A_n$ represents the histogram area that indicates the level of the distinct open state for 1 to n channels in the patch examined, and n is the number of active channels. The single channel conductance of TASK3 channels was calculated using the ratio of current amplitude of the first open state to voltage at -60 mV or +60 mV.

Ethics statement

All experiments with animals were approved by the Animal Research Committee of East China Normal University (PROTOCOL No. m20171020 and m20180112) and the Animal Research Committee of West China Hospital of Sichuan University (PROTOCOL No. 2018175A). For tissue collection, mice were given a lethal dose of pentobarbital intraperitoneally.

Animals

BALB/c mice and Sprague-Dawley rats were used in most animal studies, and TASK-3

KO mice and WT control littermates were on a C57BL/6 background. Male mice or rats aged 8-10 weeks were used for behavioral tests unless stated otherwise. Animals were housed in a conventional facility at 21 ℃ on a 12 h light-dark cycle with unrestricted access to food and water.

TASK-3 KO mice generation

To generate a *Kcnk9* knockout C57BL/6 mouse line with the CRISPR-Cas9 genome editing system, two single-guide RNAs (sgRNA-1, 5′-CCGCTTCATGGCCGCGAAGAAGG-3′, and sgRNA-2, 5′-AGGAACCGGCGAATTTCCACTGG-3′) flanking exon1 were designed (Bioray Laboratories). A 241-bp deletion was bound to exon 1 of the *Kcnk9* gene locus, resulting in *Kcnk9*$^{\Delta/\Delta}$ mice with a frameshift mutation. Additional information will be provided upon request.

Spared nerve injury model

Unilateral spared nerve injury (SNI) surgery was performed. The experimental animals were placed in the prone position. After disinfection with povidone iodide and 75% ethanol, a minimal skin incision was made at the mid-thigh level to expose the sciatic nerve and its three branches by separating the muscle layers. The tibial and common peroneal nerves were tightly ligated with 5.0 silk threads, and a 1-2 mm section was removed between the proximal and distal parts of the nerves. The sural nerve was restrictively preserved to avoid any harmful injury. The muscle layer and skin were

570 closed after surgery, and the animals were transferred to a warm pad to recover from
571 anesthesia.

572 **Chronic inflammatory pain model**

573 A volume of 20 μL Complete Freund's Adjuvant (CFA) (Sigma-Aldrich) was
574 subcutaneously injected into the left hindpaw of the mice to induce chronic inflammatory
575 pain in mice. After injection, the syringe was maintained for at least 30 s to avoid
576 overflow.

577 **Tail immersion**

578 Mice were restrained in the test tube with their tails stretching out and moving freely 15
579 min twice daily for 3 days. The distal third of the tail was immersed in a water bath at
580 5 ℃, 20 ℃, 40 ℃, 46 ℃, or 52 ℃. Three measurements of tail flick latency (in seconds)
581 to stimulation, as indicated by rapid tail flexion, were averaged. A cutoff value of 15
582 seconds was adopted to prevent unexpected damage.

583 **Formalin test**

584 Mice were housed individually in Plexiglas chambers. After habituation to the testing
585 environment for at least 30 min, the left hindpaw of the mice was injected subcutaneously
586 with formalin (20 μL of 2.5% formalin, diluted in saline), and the mice were placed into
587 the chamber of the automated formalin apparatus, where movement of the
588 formalin-injected paw was recorded by an action camera (SONY, HDR-AS50). The
589 number of paw flinches was counted at 5 min intervals for 60 min by a blind

590 experimenter. The time spent exhibiting these pain behaviors was recorded for the first
591 (0-10 min) and second phases (10-60 min).

592 **Paw pressure**

593 The effects of mechanical nociception were evaluated with an Analgesimeter (model
594 37215; Ugo-Basile, Varese, Italy). Mice were placed in the testing room for 3 continuous
595 days to acclimate to the environment. The hindpaws of mice were pressed with a constant
596 pressure of 450 g using a cone-shaped paw-presser with a rounded tip and immediately
597 released as soon as the animal showed a struggle response, and the reaction latency was
598 recorded in seconds. The analgesic effects of TASK-3 agonists were evaluated 30 min
599 after i.p. injection.

600 **Spontaneous pain test**

601 After 3 days of acclimation, the SNI mice were placed in an elevated transparent cage (20
602 × 20 × 14 cm) with a wire mesh floor (0.5 × 0.5 cm). A 5 min duration was videoed by an
603 action camera (SONY, HDR-AS50) for each mouse, and the number of left hindpaw
604 flinches was calculated by a blind experimenter.

605 **Cold plantar test**

606 Mice were allowed to acclimate to the testing environment 2-3 h daily for 3 continuous
607 days. The cold probe produced freshly with fine dry ice powder in a 5 mL syringe was
608 held against a 6 mm depth of flat glass. The center of the hindpaw was targeted, and the
609 withdrawal latency, manifesting as a quick flick or paw licking, was recorded. A cutoff

610 time of 30 s was used to prevent potential tissue damage.

611 **von Frey test**

612 The SNI rats and mice were individually placed in the chamber as described in the
613 spontaneous pain test. Mechanical sensitivity was assessed by two methods.

614 Method 1 (for all the von Frey tests described except Fig. 5D): The mechanical paw
615 withdrawal threshold was assessed using von Frey filaments with an ascending order. The
616 tip of the filament was perpendicularly targeted to the region comprising the sural nerve
617 territory, and sufficient stimulation was maintained for 1 s. Rapid paw withdrawal or
618 flinching was considered a positive response, and the bending force for which at least 60%
619 of the application elicited a positive response was recorded as the mechanical paw
620 withdrawal threshold.

621 Method 2 (up-down method): Mechanical responses were tested by stimulating the
622 region comprising the sural nerve territory with von Frey monofilaments by using the
623 up-and-down method, starting with 0.04 g. Biting, licking, and withdrawal during or
624 immediately following the 3 s stimulus were considered a positive response.

625 **Hargreaves test**

626 Hindpaw sensitivity to a noxious thermal stimulus was assessed using a radiant heat
627 source (model 37370; Ugo-Basile, Varese, Italy). The stimulus intensity was set to
628 produce an approximate latency of 10 s at baseline, and a cut-off value was set at 20 s to
629 avoid unexpected damage. Mice were allowed to acclimate in Plexiglas chambers with a

glass floor for 3 days, and the time to paw withdrawal was measured per mouse with a 5 min inter-stimulation period. Three trials were averaged to yield the withdrawal latency.

RNAscope *in situ* hybridization

The sequences of the target probes, preamplifier, amplifier and label probes are proprietary and commercially available (Advanced Cell Diagnostics). *In situ* hybridization was performed on frozen DRG sections (10 μm) using RNAscope Multiplex Fluorescent Reagent Kit v2 (ACDbio, Cat#323100) and RNAscope 4-Plex Ancillary Kit for Multiplex Fluorescent Kit v2 (ACDbio, Cat#323120). The hybridization assay was performed as described by the vendor's protocol. The *in situ* probes included *Kcnk3* (Cat#534881), *Kcnk9* (Cat#475681), *Trpa1* (Cat#400211), *Trpv1* (Cat#313331), *Trpm8* (Cat#420451), *Rbfox3* (Cat#313311), *Th* (Cat#317621), *Ntrk2* (Cat#423611), and *P2rx3* (Cat#521611). The specificity of the fluorescence signals was validated by an RNAscope 3-plex Positive Control Probe (Cat#320881) and an RNAscope 3-plex Negative Control Probe (Cat#320871). Fluorescence images were taken using a NIKON A1R^{+}MP two-photon confocal scanning microscope and were analyzed using ImageJ software.

Acutely dissociated DRG neuron preparation and electrophysiology

Three to six-week-old male Sprague-Dawley rats were sacrificed. The DRGs were collected in a 35-mm tissue culture dish and digested in 3% collagenase for 20 min, followed by 1% trypsin for another 30 min. After titrating by sucking up and down, the

650 DRG neurons were cultured in neurobasal medium containing 2% B27 medium for 2-4 h.
651 The bath solution contained (in mM) 140 NaCl, 3 KCl, 1.3 $MgCl_2$, 10 HEPES, 2.4 $CaCl_2$,
652 and 10 glucose, pH 7.3. The pipette solution contained (in mM) 40 KCl, 10 HEPES, 5
653 EGTA, 10 NaCl, 95 K-gluconate, and 4 Mg-ATP, pH 7.4. To minimize voltage-gated
654 currents, voltage ramps from -120 mV to -30 mV were applied, and 1 mM CsCl was
655 added extracellularly to block hyperpolarization-activated currents. To determine the
656 reversal potential of the CHET3-sensitive currents, NaCl was replaced with equimolar
657 KCl. Whole-cell recordings were performed with hardware settings similar to those
658 described for electrophysiology in HEK-293T cells.

659 **Acutely dissociated DRG neuron preparation and intracellular Ca^{2+} imaging**

660 Two-week-old male Sprague-Dawley rats were sacrificed. The DRGs were collected in a
661 35-mm tissue culture dish and digested in 2.5 mg/mL papain (Sigma-Aldrich) for 30 min
662 at 37 ℃, followed by 2.5 mg/mL collagenase (Sigma-Aldrich) for another 30 min.
663 Digested ganglia were gently washed with neurobasal medium and mechanically
664 dissociated by passage through the pipette. Neurons were seeded on laminin-coated wells
665 (Corning) and cultured overnight at 37 ℃ in 5% CO_2 in neurobasal medium
666 supplemented with 2% B27 (Sigma-Aldrich) and containing 50 ng/mL GDNF
667 (PeproTech) and 50 ng/mL BDNF (PeproTech).

668 Changes in intracellular Ca^{2+} concentration were monitored using ratiometric
669 Fura-2-based fluorimetry. Neurons were loaded with 2 μM Fura-2-acetoxymethyl ester

(Yeasen) dissolved in bath solution and 0.02% Pluronic F127 (Sigma-Aldrich) for 30 min at 37℃. Fluorescence was measured during alternating illumination at 340 and 380 nm using an Olympus IX73 inverted fluorescence microscopy system. The bath solution contained (in mM) 138 NaCl, 5.4 KCl, 2 $CaCl_2$, 2 $MgCl_2$, 10 glucose, and 10 HEPES, pH 7.4, adjusted with NaOH. At the end of each experiment, cells were subjected to a depolarizing solution containing 50 mM KCl, and cells nonresponsive to 50 mM KCl were excluded from the analysis. The bar graphs in Fig. 7I and fig. S15B are pooled data from both responding cells and nonresponding cells under different conditions.

Thermal stimulation

Coverslip pieces with cultured cells were placed in a recording chamber and continuously perfused (approximately 1 mL/min).

Cool stimulation: The temperature was adjusted with iced perfusion solution and controlled by a feedback device. Cold sensitivity was investigated with an ~2 min duration ramp-like temperature drop from 37 ℃ to ~15 ℃.

Heat stimulation: The temperature was adjusted with a water-heated device (model TC-324B/344B, America), with the temperature of the perfusion solution raised and controlled by a feedback device. Heat sensitivity was investigated with an ~5 min duration ramp-like temperature rise from 25 ℃ to ~43 ℃.

Statistical analysis

Statistical analyses were carried out using Origin 9.0 software (Origin Lab Corporation,

690 Northampton, USA). Data were analyzed as described in the figure legends. The
691 normality of the data distribution was determined before appropriate statistical methods
692 were chosen. The drug was assessed as significantly active by using statistical tests to
693 compare the values at baseline to those at given time points unless specified. No
694 statistical methods were used to predetermine sample sizes.
695
696 **SUPPLEMENTARY MATERIALS**
697 Materials and Methods
698 Fig. S1. A potential druggable pocket identified in several structures of K2P channels.
699 Fig. S2. Selectivity of PK-THPP against hERG, Kv2.1 and BK channels.
700 Fig. S3. Representative current traces for whole-cell recordings on several K2P channels
701 and other ion channels.
702 Fig. S4. 10 μM CHET3 does not show effect on three pain-related GPCRs.
703 Fig. S5. Binding modes of CHET3 suggested by docking and MD simulations.
704 Fig. S6. Whole-cell path-clamp current recording for three TASK-3 mutants.
705 Fig. S7. Conformations of the extracellular ion pathway in MD simulations.
706 Fig. S8. Dose-dependent analgesia by CHET3 in mechanical allodynia.
707 Fig. S9. Effects of CHET3 on the locomotion activities, blood pressure and body
708 temperature in rodents.
709 Fig. S10. Comparison of the binding of CHET3, CHET3-1 and CHET3-2.

720

721 **REFERENCES AND NOTES**

722 1. N. D. Volkow, A. T. McLellan, Opioid abuse in chronic pain—misconceptions and

723 mitigation strategies. *Eur. J. Neurosci.* **374**, 1253-1263 (2016).

724 2. A. S. Yekkirala, D. P. Roberson, B. P. Bean, C. J. Woolf, Breaking barriers to novel

725 analgesic drug development. *Nat. Rev. Drug Discov.* **16**, 544-563 (2017).

726 3. S. A. N. Goldstein, D. Bockenhauer, I. O'Kelly, N. Zilberberg, Potassium leak

727 channels and the KCNK family of two-P-domain subunits. *Nat. Rev. Neurosci.* **2**,

728 175-184 (2001).

729 4. J. Busserolles, C. Tsantoulas, A. Eschalier, J. A. Lopez Garcia, Potassium channels in

neuropathic pain: advances, challenges, and emerging ideas. *Pain* **157**, S7-S14 (2016).

5. S. G. Waxman, G. W. Zamponi, Regulating excitability of peripheral afferents: emerging ion channel targets. *Nat. Neurosci.* **17**, 153-163 (2014).
6. A. Mathie, E. L. Veale, Two-pore domain potassium channels: potential therapeutic targets for the treatment of pain. *Pflugers Arch.* **467**, 931-943 (2015).
7. Y. Kim, H. Bang, D. Kim, TASK-3, a new member of the tandem pore K^+ channel family. *J. Biol. Chem.* **275**, 9340-9347 (2000).
8. S. Rajan, E. Wischmeyer, G. X. Liu, R. P. Muller, J. Daut, A. Karschin, C. Derst, TASK-3, a novel tandem pore domain acid-sensitive K^+ channel - An extracellular histidine as pH sensor. *J. Biol. Chem.* **275**, 16650-16657 (2000).
9. T. K. Baumann, P. Chaudhary, M. E. Martenson, Background potassium channel block and TRPV1 activation contribute to proton depolarization of sensory neurons from humans with neuropathic pain. *Eur. J. Neurosci.* **19**, 1343-1351 (2004).
10. C. Morenilla-Palao, E. Luis, C. Fernández-Peña, E. Quintero, J. L. Weaver, D. A. Bayliss, F. Viana, Ion channel profile of TRPM8 cold receptors reveals a role of TASK-3 potassium channels in thermosensation. *Cell Rep.* **8**, 1571-1582 (2014).
11. D. J. Langford, C. West, C. Elboim, B. A. Cooper, G. Abrams, S. M. Paul, B. L. Schmidt, J. D. Levine, J. D. Merriman, A. Dhruva, J. Neuhaus, H. Leutwyler, C. Baggott, C. W. Sullivan, B. E. Aouizerat, C. Miaskowski, Variations in potassium

channel genes are associated with breast pain in women prior to breast cancer surgery. *J. Neurogenet.* **28**, 122-135 (2014).

12. V. Le Guilloux, P. Schmidtke, P. Tuffery, Fpocket: an open source platform for ligand pocket detection. *BMC bioinformatics* **10**, 168 (2009).
13. A. N. Miller, S. B. Long, Crystal structure of the human two-pore domain potassium channel K2P1. *Science* **335**, 432-436 (2012).
14. M. Lolicato, P. M. Riegelhaupt, C. Arrigoni, K. A. Clark, D. L. Minor, Jr., Transmembrane helix straightening and buckling underlies activation of mechanosensitive and thermosensitive K2P channels. *Neuron* **84**, 1198-1212 (2014).
15. Y. Y. Dong, A. C. Pike, A. Mackenzie, C. McClenaghan, P. Aryal, L. Dong, A. Quigley, M. Grieben, S. Goubin, S. Mukhopadhyay, G. F. Ruda, M. V. Clausen, L. Cao, P. E. Brennan, N. A. Burgess-Brown, M. S. Sansom, S. J. Tucker, E. P. Carpenter, K2P channel gating mechanisms revealed by structures of TREK-2 and a complex with Prozac. *Science* **347**, 1256-1259 (2015).
16. F. Sievers, A. Wilm, D. Dineen, T. J. Gibson, K. Karplus, W. Li, R. Lopez, H. McWilliam, M. Remmert, J. Soding, J. D. Thompson, D. G. Higgins, Fast, scalable generation of high-quality protein multiple sequence alignments using Clustal Omega. *Mol. Syst. Biol.* **7**, 539 (2011).
17. S. F. Altschul, T. L. Madden, A. A. Schäffer, J. Zhang, Z. Zhang, W. Miller, D. J. Lipman, Gapped BLAST and PSI-BLAST: a new generation of protein database

search programs. *Nucleic Acids Res.* **25**, 3389-3402 (1997).

18. M. Bertoni, F. Kiefer, M. Biasini, L. Bordoli, T. Schwede, Modeling protein quaternary structure of homo- and hetero-oligomers beyond binary interactions by homology. *Sci Rep.* **7**, 10480 (2017).

19. A. Waterhouse, M. Bertoni, S. Bienert, G. Studer, G. Tauriello, R. Gumienny, F. T. Heer, T. A. P. de Beer, C. Rempfer, L. Bordoli, R. Lepore, T. Schwede, SWISS-MODEL: homology modelling of protein structures and complexes. *Nucleic Acids Res.* **46**, W296-W303 (2018).

20. A. Šali, T. L. Blundell, Comparative protein modelling by satisfaction of spatial restraints. *J. Mol. Biol.* **234**, 779-815 (1993).

21. C. A. Coburn, Y. F. Luo, M. X. Cui, J. B. Wang, R. Soll, J. C. Dong, B. Hu, M. A. Lyon, V. P. Santarelli, R. L. Kraus, Y. Gregan, Y. Wang, S. V. Fox, J. Binns, S. M. Doran, D. R. Reiss, P. L. Tannenbaum, A. L. Gotter, P. T. Meinke, J. J. Renger, Discovery of a pharmacologically active antagonist of the two-pore-domain potassium channel K_{2P}9.1 (TASK-3). *ChemMedChem* **7**, 123-133 (2012).

22. G. Czirják, P. Enyedi, Formation of functional heterodimers between the TASK-1 and TASK-3 two-pore domain potassium channel subunits. *J. Biol. Chem.* **277**, 5426-5432 (2002).

23. C. E. Clarke, E. L. Veale, P. J. Green, H. J. Meadows, A. Mathie, Selective block of the human 2-P domain potassium channel, TASK-3, and the native leak potassium

current, IK_{SO}, by zinc. *J. Physiol.* **560**, 51-62 (2004).

24. S. Rinné, A. K. Kiper, G. Schlichthörl, S. Dittmann, M. F. Netter, S. H. Limberg, N. Silbernagel, M. Zuzarte, R. Moosdorf, H. Wulf, E. Schulze-Bahr, C. Rolfes, N. Decher, TASK-1 and TASK-3 may form heterodimers in human atrial cardiomyocytes. *J. Mol. Cell. Cardiol.* **81**, 71-80 (2015).
25. M. Schewe, H. Sun, Ü. Mert, A. Mackenzie, A. C. W. Pike, F. Schulz, C. Constantin, K. S. Vowinkel, L. J. Conrad, A. K. Kiper, W. Gonzalez, M. Musinszki, M. Tegtmeier, D. C. Pryde, H. Belabed, M. Nazare, B. L. de Groot, N. Decher, B. Fakler, E. P. Carpenter, S. J. Tucker, T. Baukrowitz, A pharmacological master key mechanism that unlocks the selectivity filter gate in K^+ channels. *Science* **363**, 875-880 (2019).
26. I. W. Davis, D. Baker, RosettaLigand docking with full ligand and receptor flexibility. *J. Mol. Biol.* **385**, 381-392 (2009).
27. G. Lemmon, J. Meiler, Rosetta Ligand docking with flexible XML protocols. *Methods Mol. Biol.* **819**, 143-155 (2012).
28. W. González, L. Zúñiga, L. P. Cid, B. Arévalo, M. I. Niemeyer, F. V. Sepúlveda, An extracellular ion pathway plays a central role in the cooperative gating of a K2P K^+ channel by extracellular pH. *J. Biol. Chem.* **288**, 5984-5991 (2013).
29. F. V. Abbott, K. B. Franklin, R. F. Westbrook, The formalin test: scoring properties of the first and second phases of the pain response in rats. *Pain* **60**, 91-102 (1995).
30. A. Tappe-Theodor, R. Kuner, Studying ongoing and spontaneous pain in

rodents-challenges and opportunities. *Eur. J. Neurosci.* **39**, 1881-1890 (2014).

31. E. Navratilova, F. Porreca, Reward and motivation in pain and pain relief. *Nat. Rev. Neurosci.* **17**, 1304-1312 (2014).

32. L. A. McWilliams, B. J. Cox, M. W. Enns, Mood and anxiety disorders associated with chronic pain: an examination in a nationally representative sample. *Pain* **106**, 127-133 (2003).

33. P. J. Turner, K. J. Buckler, Oxygen and mitochondrial inhibitors modulate both monomeric and heteromeric TASK-1 and TASK-3 channels in mouse carotid body type-1 cells. *J. Physiol.* **591**, 5977-5998 (2013).

34. J. Vriens, B. Nilius, T. Voets, Peripheral thermosensation in mammals. *Nat. Rev. Neurosci.* **15**, 573-589 (2014).

35. L. Li, M. Rutlin, V. E. Abraira, C. Cassidy, L. Kus, S. Gong, M. P. Jankowski, W. Luo, N. Heintz, H. R. Koerber, C. J. Woodbury, D. D. Ginty, The functional organization of cutaneous low-threshold mechanosensory neurons. *Cell* **147**, 1615-1627 (2011).

36. L. Vulchanova, M. S. Riedl, S. J. Shuster, L. S. Stone, K. M. Hargreaves, G. Buell, A. Surprenant, R. A. North, R. Elde, P2X3 is expressed by DRG neurons that terminate in inner lamina II. *Eur. J. Neurosci.* **10**, 3470-3478 (1998).

37. S. L. Pollema-Mays, M. V. Centeno, C. J. Ashford, A. V. Apkarian, M. Martina, Expression of background potassium channels in rat DRG is cell-specific and

down-regulated in a neuropathic pain model. *Mol. Cell. Neurosci.* **57**, 1-9 (2013).

38. H. J. Behrendt, T. Germann, C. Gillen, H. Hatt, R. Jostock, Characterization of the mouse cold-menthol receptor TRPM8 and vanilloid receptor type-1 VR1 using a fluorometric imaging plate reader (FLIPR) assay. *Br. J. Pharmacol*. **141**, 737-745 (2004).

39. M. J. Caterina, M. A. Schumacher, M. Tominaga, T. A. Rosen, J. D. Levine, D. Julius, The capsaicin receptor: a heat-activated ion channel in the pain pathway. *Nature* **389**, 816-824 (1997).

40. N. R. Gavva, R. Tamir, Y. S. Qu, L. Klionsky, T. J. Zhang, D. Immke, J. Wang, D. Zhu, T. W. Vanderah, F. Porreca, E. M. Doherty, M. H. Norman, K. D. Wild, A. W. Bannon, J. C. Louis, J. J. S. Treanor, AMG 9810 [(*E*)-3-(4-*t*-butylphenyl)-*N*-(2,3-dihydrobenzo[*b*][1,4]dioxin-6-yl)acrylamide], a novel vanilloid receptor 1 (TRPV1) antagonist with antihyperalgesic properties. *J. Pharmacol. Exp. Ther*. **313**, 474-484 (2005).

41. C. R. McNamara, J. Mandel-Brehm, D. M. Bautista, J. Siemens, K. L. Deranian, M. Zhao, N. J. Hayward, J. A. Chong, D. Julius, M. M. Moran, C. M. Fanger, TRPA1 mediates formalin-induced pain. *Proc. Natl. Acad. Sci. U.S.A.* **104**, 13525-13530 (2007).

42. J. R. Deuis, Z. Dekan, J. S. Wingerd, J. J. Smith, N. R. Munasinghe, R. F. Bhola, W. L. Imlach, V. Herzig, D. A. Armstrong, K. J. Rosengren, F. Bosmans, S. G. Waxman,

S. D. Dib-Hajj, P. Escoubas, M. S. Minett, M. J. Christie, G. F. King, P. F. Alewood, R. J. Lewis, J. N. Wood, I. Vetter, Pharmacological characterisation of the highly $Na_V1.7$ selective spider venom peptide Pn3a. *Sci Rep.* **7**, 40883 (2017).

43. E. C. Emery, A. P. Luiz, J. N. Wood, $Na_v1.7$ and other voltage-gated sodium channels as drug targets for pain relief. *Expert Opin. Ther. Targets* **20**, 975-983 (2016).

44. P. Royal, A. Andres-Bilbe, P. Á. Prado, C. Verkest, B. Wdziekonski, S. Schaub, A. Baron, F. Lesage, X. Gasull, J. Levitz, G. Sandoz, Migraine-associated TRESK mutations increase neuronal excitability through alternative translation initiation and inhibition of TREK. *Neuron* **101**, 232-245 (2019).

45. D. W. Kang, J. H. Han, E. M. Talley, D. A. Bayliss, D. H. Kim, Functional expression of TASK-1/TASK-3 heteromers in cerebellar granule cells. *J. Physiol.* **554**, 64-77 (2004).

46. A. P. Berg, E. M. Talley, J. P. Manger, D. A. Bayliss, Motoneurons express heteromeric TWIK-related acid-sensitive K^+ (TASK) channels containing TASK-1 (KCNK3) and TASK-3 (KCNK9) subunits. *J. Neurosci.* **24**, 6693-6702 (2004).

47. D. Kim, E. J. Cavanaugh, I. Kim, J. L. Carroll, Heteromeric TASK-1/TASK-3 is the major oxygen-sensitive background K^+ channel in rat carotid body glomus cells. *J. Physiol.* **587**, 2963-2975 (2009).

48. S. Pronk, S. Páll, R. Schulz, P. Larsson, P. Bjelkmar, R. Apostolov, M. R. Shirts, J. C. Smith, P. M. Kasson, D. van der Spoel, B. Hess, E. Lindahl, GROMACS 4.5: a

high-throughput and highly parallel open source molecular simulation toolkit. *Bioinformatics* **29**, 845-854 (2013).

49. J. B. Klauda, R. M. Venable, J. A. Freites, J. W. O'Connor, D. J. Tobias, C. Mondragon-Ramirez, I. Vorobyov, A. D. MacKerell, Jr., R. W. Pastor, Update of the CHARMM all-atom additive force field for lipids: validation on six lipid types. *J. Phys. Chem. B* **114**, 7830-7843 (2010).
50. P. V. Bharatam, D. S. Patel, P. Iqbal, Pharmacophoric features of biguanide derivatives: an electronic and structural analysis. *J. Med. Chem.* **48**, 7615-7622 (2005).
51. K. M. Tye, R. Prakash, S. Y. Kim, L. E. Fenno, L. Grosenick, H. Zarabi, K. R. Thompson, V. Gradinaru, C. Ramakrishnan, K. Deisseroth, Amygdala circuitry mediating reversible and bidirectional control of anxiety. *Nature* **471**, 358-362 (2011).

Acknowledgements: We thank Bioray Laboratories for technical support in preparing *Kcnk9* knockout mice. We thank Dr. Tao Li (West China Hospital) for technical assistance with blood pressure test and Miss Rongrong Cui (SIMM) for assistance on PK test. We thank the supports of ECNU Multifunctional Platform for Innovation (001 and 011).

Funding: This work was funded by National Science & Technology Major Project “Key New Drug Creation and Manufacturing Program” of China (2018ZX09711002 to H.J.,

Q.Z., and H.Y.), the National Natural Science Foundation of China (21422208 to H.Y; 31600832 to R.J.), Thousand Talents Plan in Sichuan Province (to R.J.), 1.3.5 Project for Disciplines of Excellence (ZY2016101), West China Hospital, Sichuan University (to J.L.), the "XingFuZhiHua" funding of ECNU (44300-19311-542500/006), the Fundamental Research Funds for the Central Universities (to H.Y., and 2018SCUH0086 to R.J.) and the Special Program for Applied Research on Super Computation of the NSFC-Guangdong Joint Fund (the second phase) under Grant No.U1501501, and the State Key Laboratory of Bioorganic and Natural Products Chemistry. **Author contributions:** P.L. performed behavior tests, ISH, Ca^{2+} imaging; Y.Q. performed drug design and computations; Y.M. performed mouse genetics on TASK-3 KO mice and behavior tests; J.F. performed electrophysiology; Z.S. performed electrophysiology, behavior tests, ISH; L.H. performed electrophysiology; S.B., Y.W. and B.S. performed Ca^{2+} imaging; J.Z. and W.G.L. performed elevated plus maze tests; Z.C. and N.P. assisted with behavior tests and cell culture; E.S. performed dark/light box tests; L.Y. assisted with behavior tests; F.T., X.L. and Z.G. performed electrophysiology for some of the initial compound screenings; P.S., Y.C. and Y.M. performed pharmacokinetics study; D.H. performed the qPCR experiments for TASK-3 KO mice; L.Z. performed experiments of μOR; D.Y. performed experiments of 5-HT_{1B}R; W.L. performed experiments of CB_1R; T.Y., J.X. and Y.M. performed experiments of echocardiography. Q.Z. prepared the derivatives of CHET3. J.L. oversaw the animal behavior tests. H.J. oversaw the

910 computations. R.J. and H.Y. initiated, supervised the project, analyzed the experiments,
911 and wrote the manuscript with input from all co-authors. **Competing interests:** The
912 authors declare no competing interests. **Data and materials availability:** All data is
913 available in the main text or the supplementary materials.
914
915
916
917
918
919
920
921
922
923
924
925
926
927
928
929

Figures

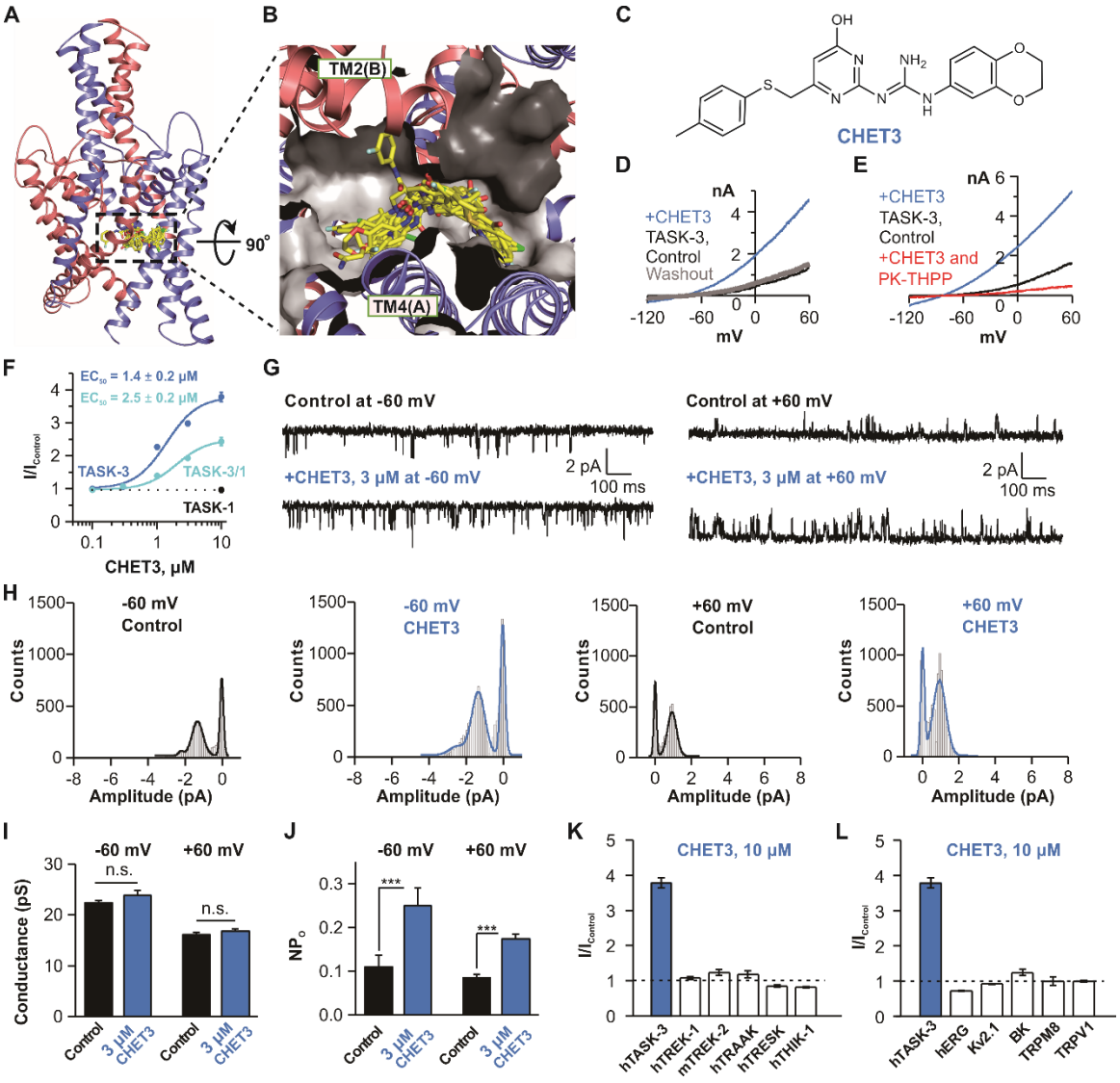

Fig. 1. Structure-based ligand discovery of CHET3.

(**A**) Pocket in a TASK-3 homology model used for virtual screening. Representative docking poses were shown. **(B)** Cytoplasmic expanded view of the pocket and the docking poses. (**C**) Chemical structure of CHET3. (**D** and **E**) Exemplar whole-cell path-clamp recordings showing the activation of TASK-3 by 10 μM CHET3 and blockade of 0.5 μM PK-THPP. (**F**) CHET3 dose-response curves for TASK-3 (n = 7) and

TASK-3/TASK-1 (n = 5). (**G**) Representative single-channel current traces from inside-out patches showing the activation of TASK-3 by CHET3 at -60 mV and +60 mV. (**H**) Histograms of the single-channel currents which were fitted by Gaussian distributions. (**I** and **J**) Analysis of conductance changes and NP_o (channel number times open probability) changes from the single-channel currents (n = 9; paired *t* test). (**K**) Summary for the effects of CHET3 on several other K2P channels (n = 7-10). (**L**) Summary for the effects of CHET3 on hERG, Kv2.1, BK, TRPM8 and TRPV1 channels (n = 5-7). Data in (F, I to L) are shown as mean ± SEM. **P* < 0.05, ***P* < 0.01, ****P* < 0.001.

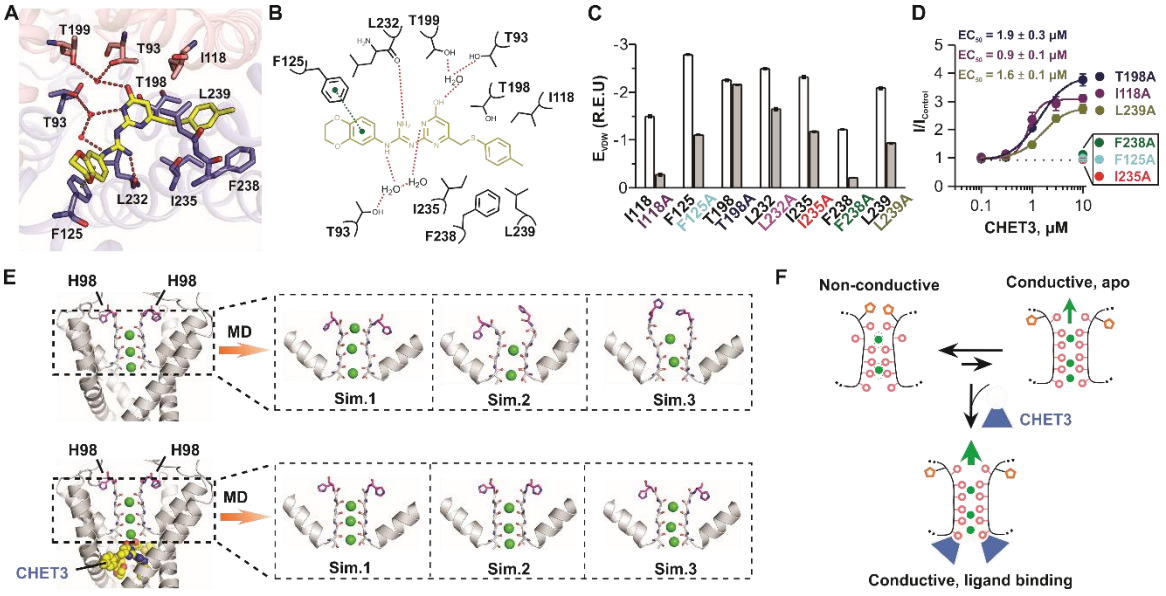

Fig. 2. Activation mechanism of CHET3 on TASK-3.

(**A** and **B**) 3-dimentional and 2-dimentional diagrams showing interactions between CHET3 and TASK-3. Hydrogen bond (red dash) and π-π interaction (green dash) were shown. (**C**) Computations showing the contributions of seven residues and their mutations to CHET3 binding. Energy unit is Rosetta Energy Unit (R.E.U.). (**D**) Dose-response curves of six mutations on CHET3 activity (n = 6). Data are shown as mean ± SEM. (**E**) Selectivity filter conformations of the *apo* TASK-3 and the CHET3-bound TASK-3 revealed by MD simulations, including bound potassium ions (green spheres), carbonyl oxygen (red sphere) rotation of filter residues, and movements of residue H98 (purple sticks). (**F**) Schematic representation of the action mechanism of CHET3 on TASK-3.

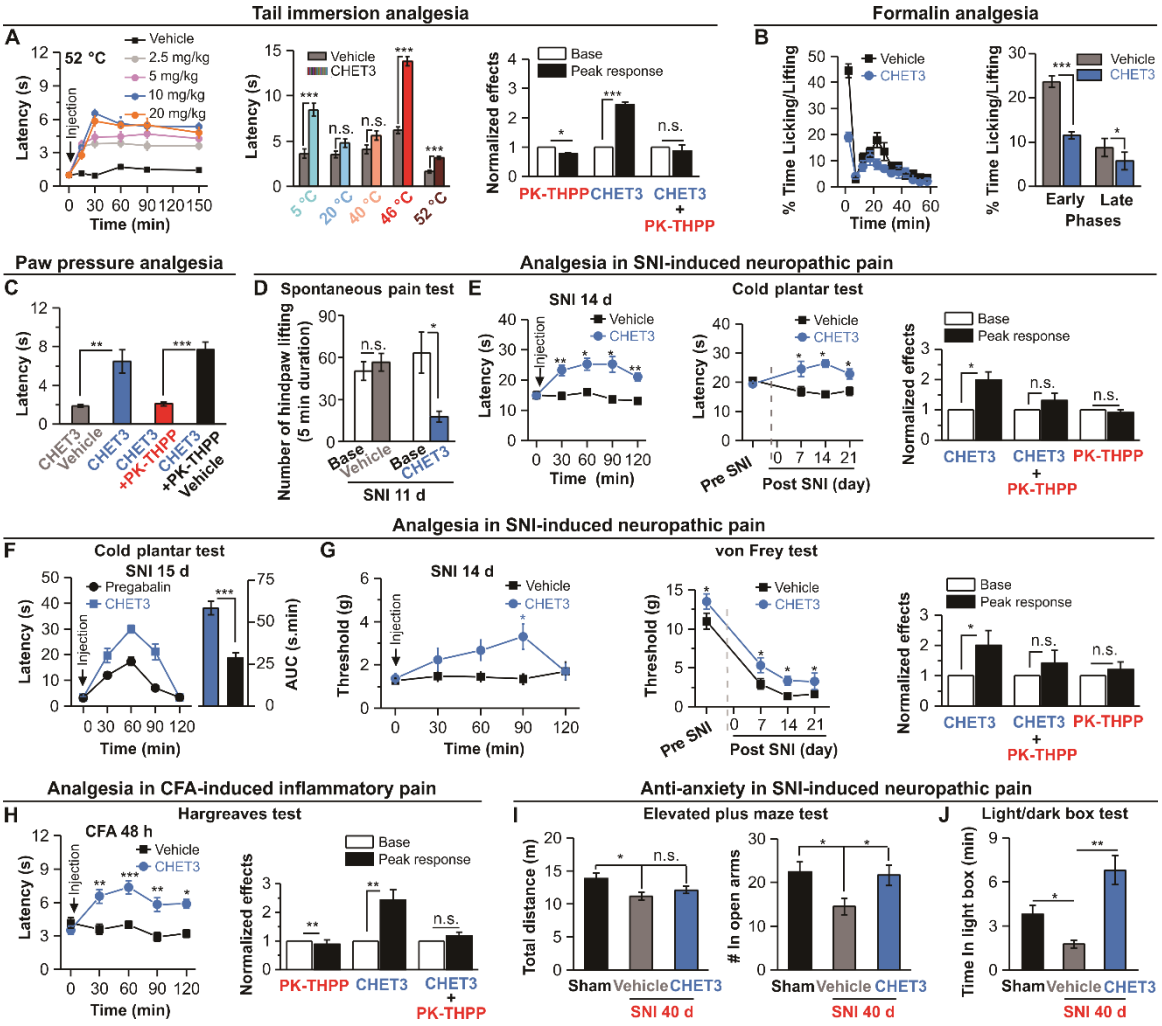

Fig. 3. Analgesic effects of CHET3 in rodents.

(**A**) *left*, Time profile for dose-dependent analgesia by CHET3 in tail immersion test at 52 °C (n = 6-10); *middle*, CHET3 analgesia in tail immersion tests at different temperatures (n = 9-11; unpaired *t* test); *right*, Summary for PK-THPP effects (n = 8-10; unpaired *t* test). (**B**) Summary for CHET3 analgesia in formalin (2.5%, 20 μl) test (n = 8; unpaired *t* test). (**C**) CHET3 and PK-THPP on the paw withdrawal latency in paw pressure test (measured at 45 min post injection, n = 8-10; paired *t* test). (**D**) CHET3 on spontaneous pain within a 10 min duration in mice (measured at 35 min post injection, n

975 = 6-10; unpaired *t* test). (**E**) *left*, Time profile for CHET3 on cold hyperalgesia in mice (n
976 = 10-11; paired *t* test); *middle*, Summary for CHET3 on cold hyperalgesia at different
977 stages in SNI (n = 9-11; unpaired *t* test); *right*, Summary for PK-THPP (n = 10; paired *t*
978 test). (**F**) Comparison of CHET3 and Pregabalin (30 mg/kg, i.p.) in cold plantar test in
979 mice (n =11-12; unpaired *t* test). (**G**) *left*, Time profile for CHET3 in mechanical
980 allodynia in rats (n = 8-13; paired *t* test); *middle*, Summary for CHET3 on mechanical
981 allodynia at different stages in SNI rats (n = 8-13; paired *t* test); *right*, Summary for
982 PK-THPP effects (n = 8; paired *t* test). (**H**) *left*, Time profile for CHET3 on heat
983 hyperalgesia (n = 10-11; paired *t* test); *right*, Summary for PK-THPP effects (n = 11;
984 paired *t* test). (**I** and **J**) CHET3 on anxiety-like behaviors in elevated plus maze test (I) (n
985 = 8-9; unpaired *t* test) and in light/dark box tested (J) (n = 6-8; unpaired *t* test). CHET3
986 (10 mg/kg) and PK-THPP (15 mg/kg) were administrated via i.p. injections unless
987 specified. Data are shown as mean ± SEM. $*P < 0.05$, $**P < 0.01$, $***P < 0.001$. n.s.,
988 not significant.
989
990

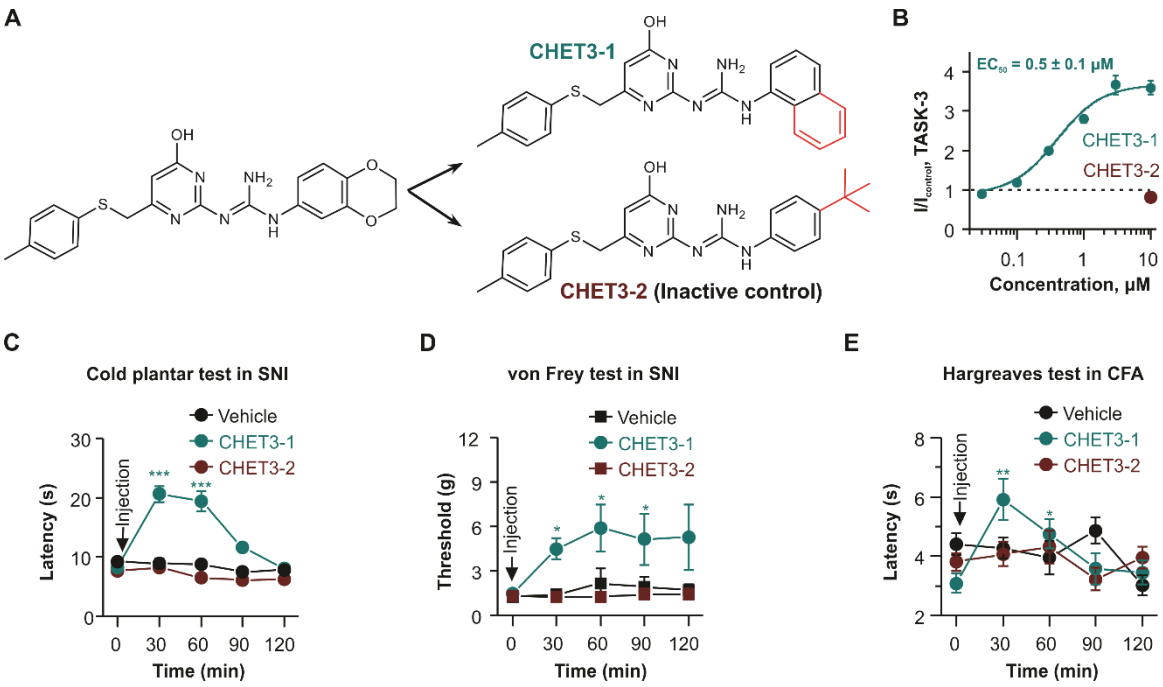

991

992 **Fig. 4. Validation of TASK-3 as analgesic target by using CHET3 derivatives.**

993 (**A**) Chemical structures of CHET3 derivatives. (**B**) Dose-response relationships for

994 CHET3-1 (n = 6) and CHET3-2 (n = 7) on TASK-3. (**C** to **E**) CHET3-1 and CHET3-2 in

995 cold hyperalgesia (C) (n = 9-11; paired *t* test), mechanical allodynia (D) (n = 7-8; paired *t*

996 test), and heat hyperalgesia (E) (n = 9-10; paired *t* test). Data are shown as mean ± SEM.

997 **P* < 0.05, ***P* < 0.01, ****P* < 0.001.

998

999

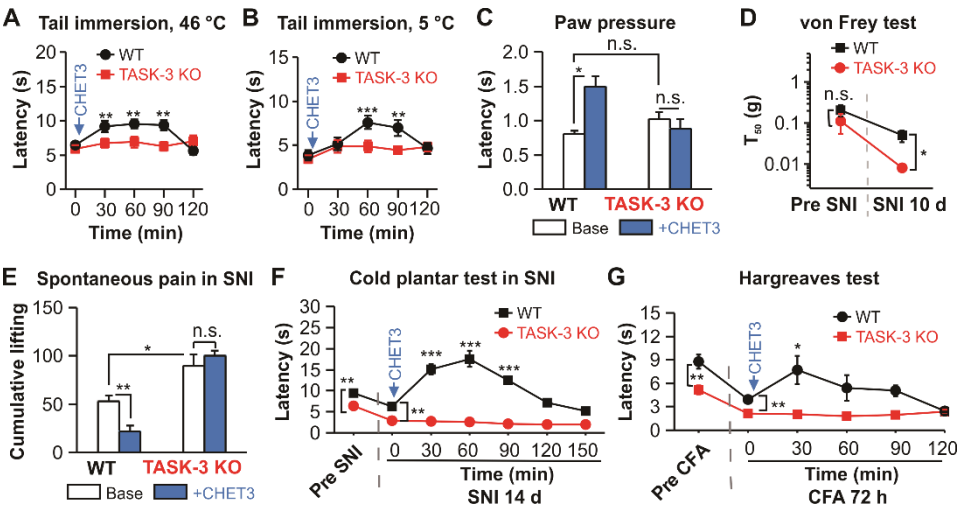

Fig. 5. Effects of systemic administration of CHET3 on TASK-3 KO mice.

(**A** and **B**) CHET3 had no analgesic effects in tail immersion tests in TASK-3 KO mice (n = 9-12; paired *t* test). (**C**) CHET3 had no analgesic effect in paw pressure tests in TASK-3 KO mice (n = 8 for KO, n = 7 for WT; paired *t* test). Note that no change of baseline sensitivity in nociception for TASK-3 KO mice in A to C. (**D**) TASK-3 KO mice in SNI model exhibited enhanced mechanical allodynia (up-down method, n = 8 for KO, n = 10 for WT; unpaired *t* test). (**E**) TASK-3 KO mice in SNI model exhibited enhanced spontaneous pain activities which was insensitive to CHET3 (n = 6-7; paired *t* test). (**F** and **G**) CHET3 had no analgesic effect in cold plantar test (n = 6-7; paired *t* test) in SNI model and Hargreaves test (n = 8-12; paired *t* test) in CFA model in TASK-3 KO mice. Note that TASK-3 KO mice had shorter paw withdraw latencies in both tests (unpaired *t* test) in base conditions. Data are shown as mean ± SEM. **P* < 0.05, ***P* < 0.01, ****P* < 0.001. n.s., not significant.

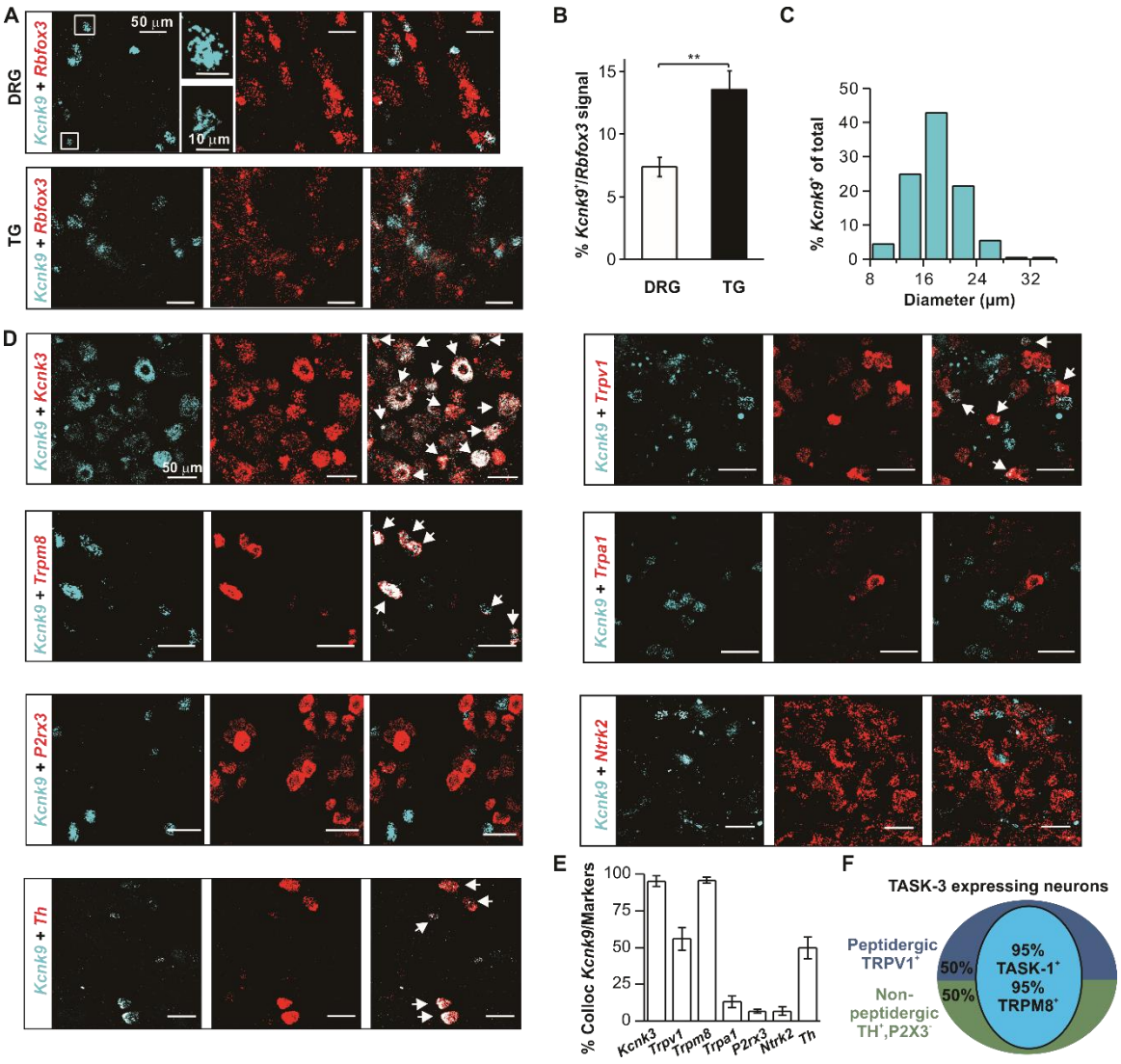

Fig 6. Distribution of TASK-3 in DRG neurons.

(**A** and **B**) Images and quantifications showing *Kcnk9* expression in sensory neurons using RNAscope (n = 7 sections from 3 mice) and TG (n = 8 sections from 3 mice) (Mann-Whitney test). Data in (B) are shown as mean ± SEM. (**C**) Quantification of the cell sizes of *Kcnk9*$^+$ neurons (n = 6 sections from 3 mice). (**D**) Representative images showing *Kcnk9*$^+$ neurons expression in different subtype of DRG neurons using RNAscope. (**E**) Bar graph summary for experiments in (D) (n = 4-9 DRG sections from

3-8 mice for each condition). Data are shown as mean ± SEM. (**F**) Schematic summary for the distribution of *Kcnk9*$^{+}$ neurons in DRG. $^{**}P < 0.01$.

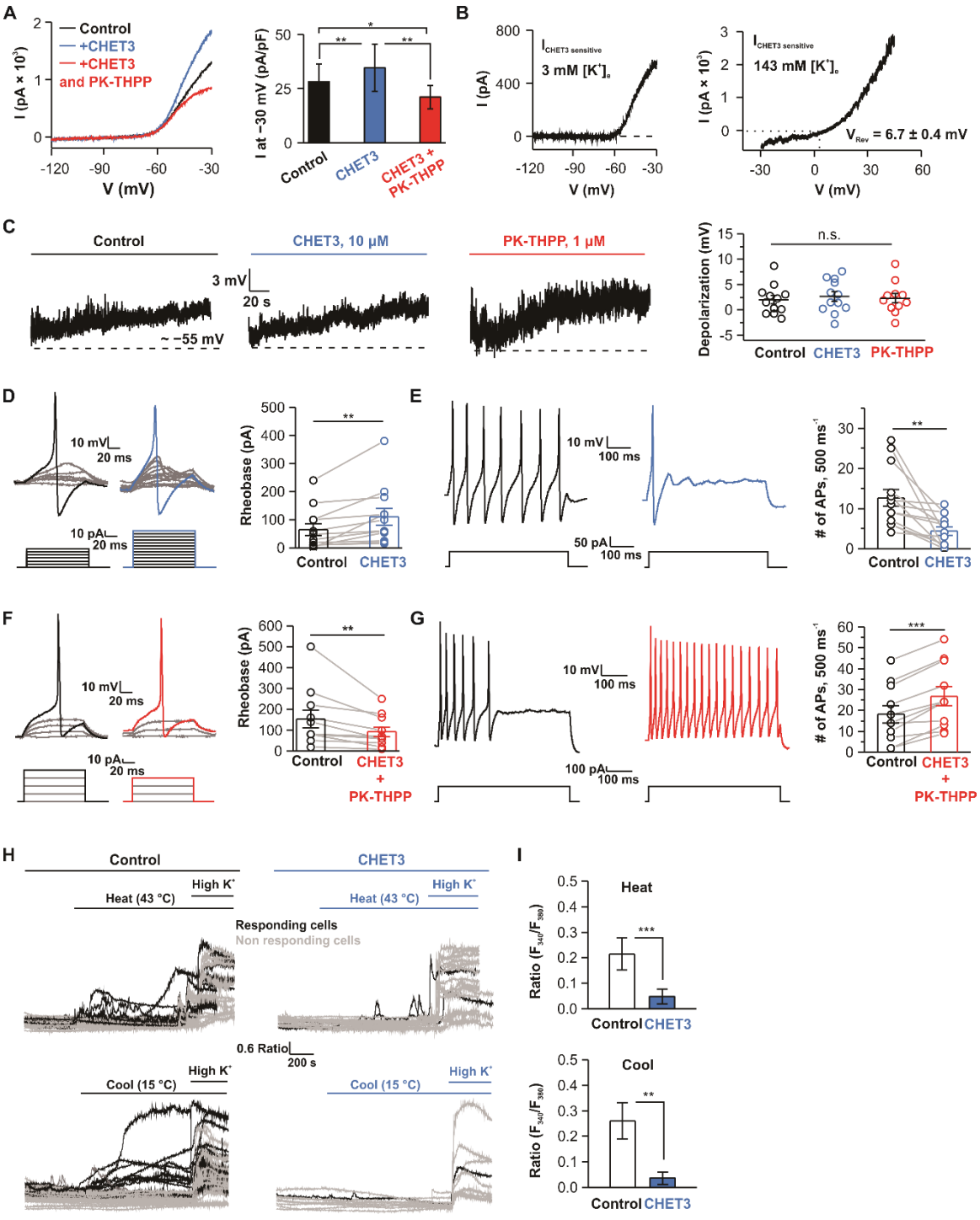

Fig 7. Functional roles of TASK-3 in nociceptive neurons.

(**A**) *left*, Representative electrophysiological traces showing CHET3 (10 µM) and PK-THPP (1 µM) effects on K^+ currents in DRG neurons; *right*, Bar graph summary for

experiments in *left* (n = 9 cells in 6 mice; paired *t* test). (**B**) Representative traces showing CHET3-sensitive currents at different extracellular K^+ concentrations (V_{Rev} was determined from n = 5 cells in 3 mice). (**C**) Representative traces and scatter plots showing resting membrane potential (RMP) changes in response to Vehicle, CHET3 or PK-THPP (n = 12 cells for Control and CHET3, n = 11 cells for PK-THPP in 5 mice for each condition; one-way ANOVA test). (**D** and **E**) Traces and bar graph showing CHET3 effect on rheobase and firing frequency in nociceptive neurons (n = 12 cells in 5 mice; paired sample Wilcoxon signed rank test in (D), paired *t* test in (E)). (**F** and **G**) Traces and bar graph showing co-application of CHET3 and PK-THPP on rheobase and firing frequency in nociceptive neurons (n = 11 cells in 3 mice; paired sample Wilcoxon signed rank test in (F), paired *t* test in (G)). (**H**) Individual Ca^{2+} imaging traces from small-sized DRG neurons in representative field of views in response to heat (25 ℃-43 ℃) , cooling (37 ℃-15 ℃). (**I**) Bar graphs summary for experiments in (H) (Heat: n = 143 cells in 11 coverslips for control, n = 99 cells in 9 coverslips for CHET3; Mann-Whitney test. Cool: n = 87 cells in 9 coverslips for control, n = 46 cells in 9 coverslips for CHET3; Mann-Whitney test. Both experiments were from 3 independent preparations from 6 mice). Data are shown as mean ± SEM. **P* < 0.05, ***P* < 0.01, ****P* < 0.001. n.s., not significant.